Controlled properties of perovskite oxide films by engineering oxygen octahedral rotation
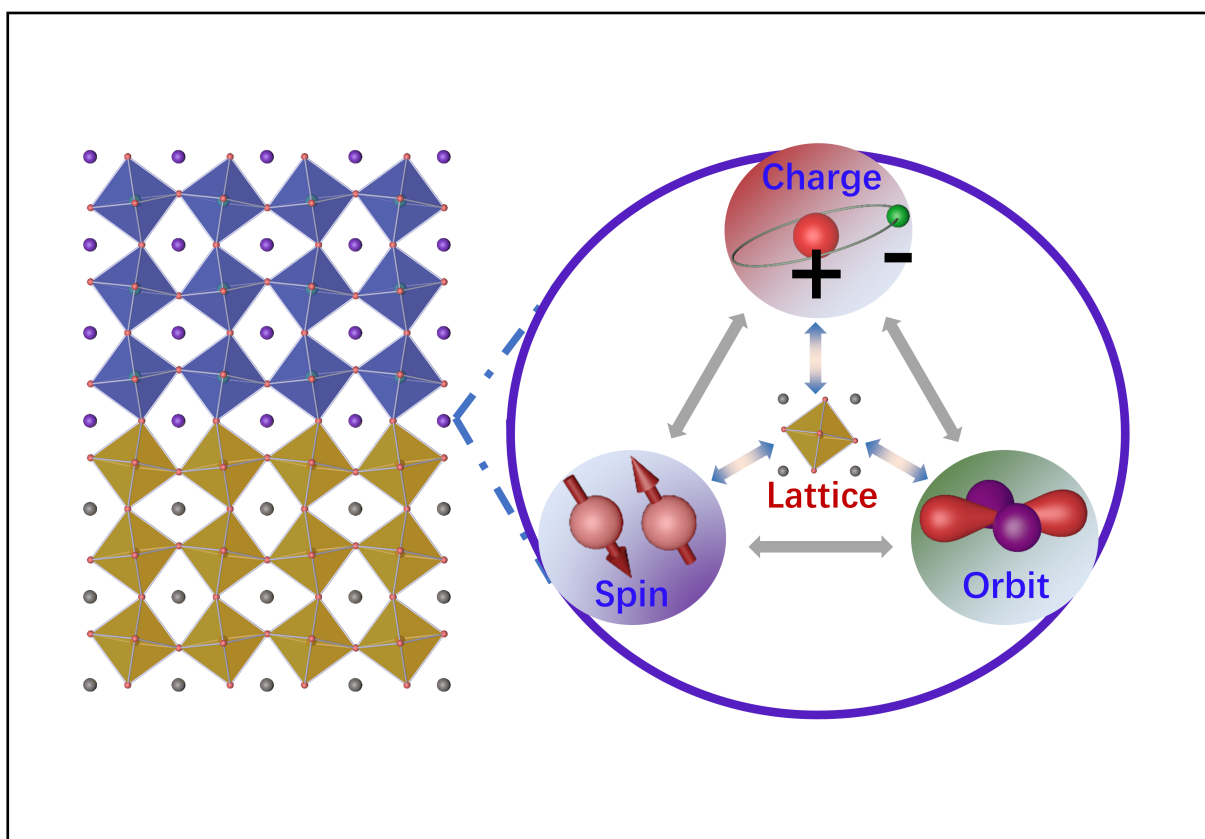
Junhua Liu, Xiaofei Gao, Wen Xiao, Shilin Hu, Yaoyao Ji, Lin Li, Kai Chen, and Zhaoliang Liao ✉

National Synchrotron Radiation Laboratory, University of Science and Technology of China, Hefei 230026, China

✉Correspondence: Zhaoliang Liao, E-mail: zliao@ustc.edu.cn

Graphical abstract

Interaction between oxygen octahedral rotation (lattice) and many degrees of freedom including spin, orbit, and charge.

Public summary

■ We review and summarize the structure of perovskite oxides, the characterization methods of oxygen octahedral rotation, as well as the response for transport, electrical polarization, and magnetism.

■ Half-order X-ray diffraction and STEM (HAADF and ABF) are two most common techniques to characterize the octahendral rotation.

■ Several key issues that need to be solved urgently are proposed to facilitate breakthroughs in octahedral-rotation-based devices.

Controlled properties of perovskite oxide films by engineering oxygen octahedral rotation

Junhua Liu, Xiaofei Gao, Wen Xiao, Shilin Hu, Yaoyao Ji, Lin Li, Kai Chen, and Zhaoliang Liao ✉

National Synchrotron Radiation Laboratory, University of Science and Technology of China, Hefei 230026, China

✉Correspondence: Zhaoliang Liao, E-mail: zliao@ustc.edu.cn

Abstract: Complex perovskite oxides exhibit extremely rich physical properties in terms of magnetism, electrical transport, and electrical polarization characteristics due to the competition and coupling of many degrees of freedom. The B-site ions and O ions in perovskite form six-coordinated octahedral units, which are connected at a common vertex toward the basic framework of the perovskite oxide, providing a crucial platform to tailor physical properties. The rotation or distortion of the oxygen octahedra will tip the competing balance, leading to many emergent ground states. To further clarify the subtle relationship between emergent properties and oxide octahedral behavior, this article reviews the structure of perovskite oxides, the characterization methods of oxygen octahedral rotation and the response of transport, electrical polarization and magnetism of several typical perovskite heterostructures to oxygen octahedral rotation modes. With knowledge of how to manipulate the octahedral rotation behavior and regulate the physical properties of perovskite oxides, rationally designing the sample manufacturing process can effectively guide the development and application of novel electronic functional materials and devices.

Keywords: perovskite oxide; interface coupling; oxide octahedral rotation; structural characterization; property regulation

CLC number: O469　　　　**Document code:** A

1　Introduction

Perovskite oxide, with the general chemical formula ABO_3, has achieved a series of important applications in low-power electronics, information storage, and energy conversion due to its extremely rich physical properties[1–3]. The d-orbital of the B-site element collaborating with charge, spin, and lattice gives rise to many interesting emergent phenomena, including multiferroic, superconductivity, metal-insulator transition, and charge/spin/orbital order[4]. Different from conventional semiconductors, perovskite oxide possesses several tunable degrees of freedom in terms of geometric structure, including typical $[BO_6]$ octahedral rotation and distortion. Recent studies have demonstrated a strong correlation between the oxide octahedral rotation (OOR) behavior and lattice vibration mode[5, 6], affording us the ability to tune or design the acoustic and optical properties of a material by OOR. More importantly, the OOR can modify the space symmetry around the heterointerface between different perovskites[7]. Lattice strain that originates from self-adapting B–O bond length is a significant approach to engineer properties and is a key mechanism to understand interface mismatch as well. However, the B–O–B bond angle changes, driven by symmetry mismatch at a heterointerface, have great potential to modulate the properties of complex oxides. The former dominates the breathing and shape distortion of the octahedra, while the latter induces octahedral rotation or tilt. Both of them can change the bandwidth of the d-band to control the electrical and magnetic properties of a material. Therefore, exploring the way to con-trol oxygen octahedral rotation and understanding the response of properties to octahedral behavior are crucial for designing novel functional materials and electronic devices.

In recent decades, with the rapid development of advanced thin film preparation and characterization techniques, including molecular beam epitaxy (MBE) and pulsed laser deposition (PLD), many atomic-level precise epitaxial heterostructures have been achieved. In fact, changing the interfacial octahedral geometry as a class of significant strategies toward interfacial emergent phenomena has gained great attention in recent years. A series of emergent phenomena[8–11], such as interfacial metallicity, superconductivity, and ferromagnetism which are not energetically favored in bulk materials, were observed at oxide interfaces. First-principles calculations demonstrated that the octahedral rotation pattern can diffuse into the interior of an epitaxial layer due to interfacial bonding, which finally produces different symmetry from the bulk counterpart[12]. Experimentally, octahedral coupling and rotation at a heterointerface were observed by some modern characterization methods, such as synchrotron radiation half-order X-ray diffraction (HO-XRD) and high-resolution scanning transmission electron microscopy (STEM)[13–15]. Realizing oxygen octahedral rotation in oxide films utilizing interfacial bonding, therefore, is considered to be a preferred strategy for tuning the physical properties of oxide systems, including but not limited to ferroelectric polarization arising from broken inversion symmetry, magnetic and transport modulation caused by the bond angle change, and the

charge/orbital order originating from the distorted oxygen octahedra[16–20]. These phenomena imply the huge potential of controlling OOR for exploring physical properties and developing novel electronic devices.

In summary, the oxygen octahedral rotation, as one key structural degree of freedom in perovskite oxide materials, has played an important role in tuning the properties of materials. In view of this, the recent progress in manipulating the electrical and magnetic properties by designing oxygen octahedral rotation is reviewed here. First, the structure characterization of perovskite oxides, the rotation mode, and the characterization methods of oxide octahedra are summarized in Section 2. Then, Section 3 shows some examples for controlling the physical properties of perovskite oxides by octahedral rotation, including electro- and magnetic- transport, electric polarization, and magnetism. In Section 4, a brief discussion of current challenges and several key problems to be solved urgently for developing devices based on octahedral rotation are proposed.

2 Complex geometric structures and characterization technologies

2.1 Structure of perovskite

Perovskite oxide is a transition metal compound with ABO_3 stoichiometry, where the A-site ion is a rare earth or alkaline earth element with a large ionic radius, and the B site is occupied by a transition metal ion with d electrons. The standard perovskite structure is skeletonized by a cubic network of $[BO_6]$ octahedra connected by common vertex O, and the A-site ion occupies the center of the cubic, with a simple cubic space group $Pm\bar{3}m$. However, varying the radius of the A-site ion or B-site ion will lead to lattice distortion, including octahedral shape distortion and rotation/tilt of octahedra, as a result of changing the local symmetry[21–23]. Fig. 1a shows a 3D schematic diagram of the octahedral connection in per-

ovskites with rotation mode ($a^+a^-a^-$). The tolerance factor[24]

$$t = \frac{R_A + R_O}{\sqrt{2}(R_B + R_O)},\qquad(1)$$

is an empirical parameter for describing the symmetry of a system to scale the crystal distortion, where R_A, R_B, and R_O represent the ionic radius of the A-site ion, B-site ion, and coordinated O ion, respectively. For an ideal perovskite, the tolerance factor $t = 1$, and the systems with $t > 1$ or $t < 1$ instead reflect an increased (hexagonal lattice) or decreased symmetry (orthorhombic or rhombohedral lattice), respectively. Filip et al.[25] introduced the octahedral factor $\mu = R_B/R_X$ (where R_B and R_X are the radius of the B-site and the ligand X, respectively) to describe the stability of $[BX_6]$ octahedra, which predicted 90000 perovskite compounds by ($t + \mu$) combination calculation. Bartel et al.[26] further developed a more accurate tolerance factor

$$\tau = \frac{R_X}{R_B} - n_A\left(n_A - \frac{R_A/R_B}{\ln(R_A/R_B)}\right),\qquad(2)$$

to predict and understand the stability of perovskite compounds (where n_A is the valence of the A-site ion), and it is considered that such perovskite compounds exist when $\tau < 4.18$. Modern characterization methods, such as STEM and HO-XRD are used to understand the microstructure of perovskite oxide heterojunctions[27–29] and the correspondence between octahedra behavior (such as rotation, distortion, etc.) and physical properties, clarifying the importance of interfacial modulation of octahedral behavior at the microscopic level.

2.2 Octahedral coupling and rotation modes

Glazer proposed 23 modes to characterize the OOR of perovskite oxides[30]. The oxygen octahedra rotate around different tilt axes. The different amplitudes of rotation are marked by a, b, and c, where a < b < c. The same letters are used to
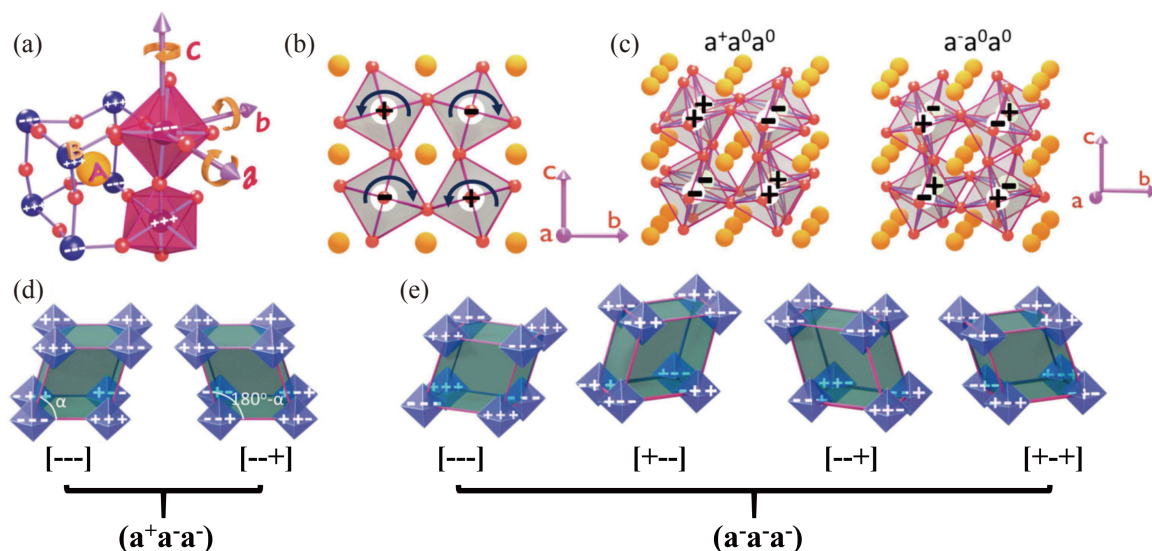
Fig. 1. Schematic diagram of octahedral network in perovskite. (a) The definition of the rotation sign of an individual octahedron in an ABO_3 perovskite unit cell with clockwise (+) and anticlockwise (−), the view direction is along the pseudocubic axis a, b, or c. (b) Rotation sign and pattern of octahedra in a shared rotation axis normal the plane. (c), (d), and (e) indicate a series of possible octahedral rotation structure network for simple ($a^+a^0a^0$)/ ($a^-a^0a^0$) modes and complex ($a^+a^-a^-$)/ ($a^-a^-a^-$) modes. Figure taken from Ref. [31].

indicate equal rotation. For example, the mode (abb) means equal rotation around axes [010] and [001] but larger than that around [100]. Mode (abc) represents different rotation amplitudes around axis [100], [010], and [001]. OOR phases are denoted by superscripts "+", "−", and "0". Here, the superscript "+" indicates that all octahedra rotate in phase, i.e., in the same direction around a given crystal axis, and the superscript "−" indicates that all octahedra rotate out of phase, i.e., neighboring octahedra rotate in the opposite direction above a given axis. The superscript "0" indicates that there is no tilt.

According to the Glazer notation, the ideal cubic perovskite has a rotation mode ($a^0 a^0 a^0$). To maintain the connectivity of the octahedra, two rules should be enforced for a rotation network. As shown in Fig. 1b, opposite rotation signs are required about the tilt axis normal to their shared plane, otherwise, the connectivity of the octahedra is broken. On the other hand, the rotation signs of adjacent octahedra around the shared axis are either in-phase or out-of-phase rotation. For example, in an ($a^+ a^0 a^0$) rotation system, all octahedra around the [100] axis possess the same sign of rotation but no rotation around others to comply with the requirement of in-phase rotation. If the rotation behavior is out-of-phase between two adjacent octahedra, then it will have opposite rotation signs ($a^- a^0 a^0$). With these two rules, the rotation networks can be produced for the ($a^+ a^0 a^0$) and ($a^- a^0 a^0$) single tilt systems, as shown in Fig. 1c.

To study the local characterization of interfacial octahedral networks, it is necessary to accurately describe the rotation of a single octahedron. A new notation [x, y, z] (where x, y, z take "+", "−", or "0") was proposed to describe the rotation of a single octahedron in our previous work[31]. Counterclockwise rotation around a specific pseudocubic axis is defined as "+", clockwise rotation is defined as "−", and no rotation is defined as "0" for a single oxygen octahedron. Therefore, for the octahedral network on the left in Fig. 1d, the front and rear octahedral arrays have exactly the same behavior considering only the in-phase rotation around the [100] axis. It should be noted that the superscript in the Glazer notation is used to represent the relative rotation direction of adjacent octahedra while the notation here is used to describe the absolute rotation direction of a single oxygen octahedron.

Using this notation, different octahedral behaviors described by the same Glazer notation can be reflected. As shown in Fig. 1d, ($a^+ a^- a^-$) can give two kinds of octahedral networks [− − −] and [− − +], which correspond to two mirror-symmetric orthogonal structures with unit cell angles α and $180° − \alpha$, respectively. The NdGaO$_3$(NGO) crystal is an example with two domain structures indicated by $\alpha < 90°$ and $\alpha > 90°$. In addition, ($a^- a^- a^-$) gives a total of four octahedral networks, namely [− − −] , [+ − −], [− − +], and [+ − +], and these octahedral networks are grouped into two pairs of rhombohedral structures, in which each pair is mirror isomeristic to each other (Fig. 1e). At the perovskite interface with the same symmetry, such as CaTiO$_3$/NdGaO$_3$ and SrRuO$_3$/DyScO$_3$, the requirement of matched OOR modes results in a single domain structure[31, 32]. For heterostructure systems with different symmetries, the symmetry of the substrate can be introduced in the film through interface OOR coupling. Using

La$_{2/3}$Sr$_{1/3}$MnO$_3$ (LSMO) thin films epitaxially grown on (110) NGO substrates as an example[33], the OOR coupling at the interface will lead to the rearrangement of oxygen rotation in LSMO (see Fig. 2a). The OOR of LSMO possesses the same rotation phases as NGO; as a result, the LSMO which in bulk is ($a^- a^- a^-$) becomes ($c^+ a^- a^-$). Due to the interface reconstruction of symmetry, the ultrathin LSMO possesses dramatically different magnetic anisotropy than the thick counterpart. Additionally, introducing a single unit cell of STO can locally modify the symmetry by tailoring the interface decay distance of the OOR (see Fig. 2b).

2.3 Characterization of oxygen octahedral rotation

With the rapid development of theoretical packets and experimental techniques, precise characterization of the modes and amplitudes of OOR has become feasible. Theoretical calculations revealed the details of OOR intuitively by optimizing the interface structure to predict the corresponding physical properties[34–37]. In experiments, the oxygen octahedral rotation can be characterized indirectly or directly by HO-XRD and STEM (including annular bright field image (ABF) and high-angle annular dark field image (HAADF))[13, 32, 33, 38–40], respectively. However, due to the small scattering factor of ligand oxygen, synchrotron X-ray, or aberration-corrected STEM is usually required to ensure high resolution.

The X-ray diffraction peaks of crystals are integers in the octahedral network without rotation, but half-integer peaks appear for the rotational system. In fact, an additional second-order period with a double lattice constant is added to the interfacial octahedral array, according to the two rules mentioned above. The corresponding half-integer diffraction peaks can be observed using the HO-XRD technique, where the position of the peak is used to determine the rotation mode, and the peak intensity is used to estimate the magnitude of the rotation[7, 29]. Specifically, when the oxygen octahedra show in-phase rotation around the pseudocubic axis [100], [010], or [001], 1/2 (even, odd, odd), 1/2 (odd, even, odd), or 1/2 (odd, odd, even) diffraction peaks will appear in the scan patterns. However, only 1/2 (odd, odd, odd) diffraction peaks are present if the OOR mode is out-of-phase. Kan et al.[41] systematically characterized the OOR in SrRuO$_3$ (SRO)/NGO heterostructures from a three-dimensional perspective using HO-XRD and quantified the dependence between HO-XRD intensity and OOR amplitude. Lee et al.[13] realized the OOR amplitude regulation of the functional layer BFO with the ($a^- b^- c^-$) mode through the symmetry design of the template SRO (T-SRO and M-SRO).

However, HO-XRD can solely reflect the global structural information at the penetration depth scale. Therefore, it cannot be used for characterizing the octahedral rotation patterns of different compounds in a multilayer oxide. To parse the OOR spatially, Chen et al.[42] recently developed an A-site ionic symmetry correlated X-ray reciprocal space mapping (RSM) technique. The out-of-phase OOR removes the orthogonality between the corresponding axes of the cation lattice, leading to the asymmetric diffraction pattern recorded by RSM. For example, in a system with the "+ − −" mode (only the rotation mode index is shown here), the orthogonality between the b axis and c axis is lifted. As shown in
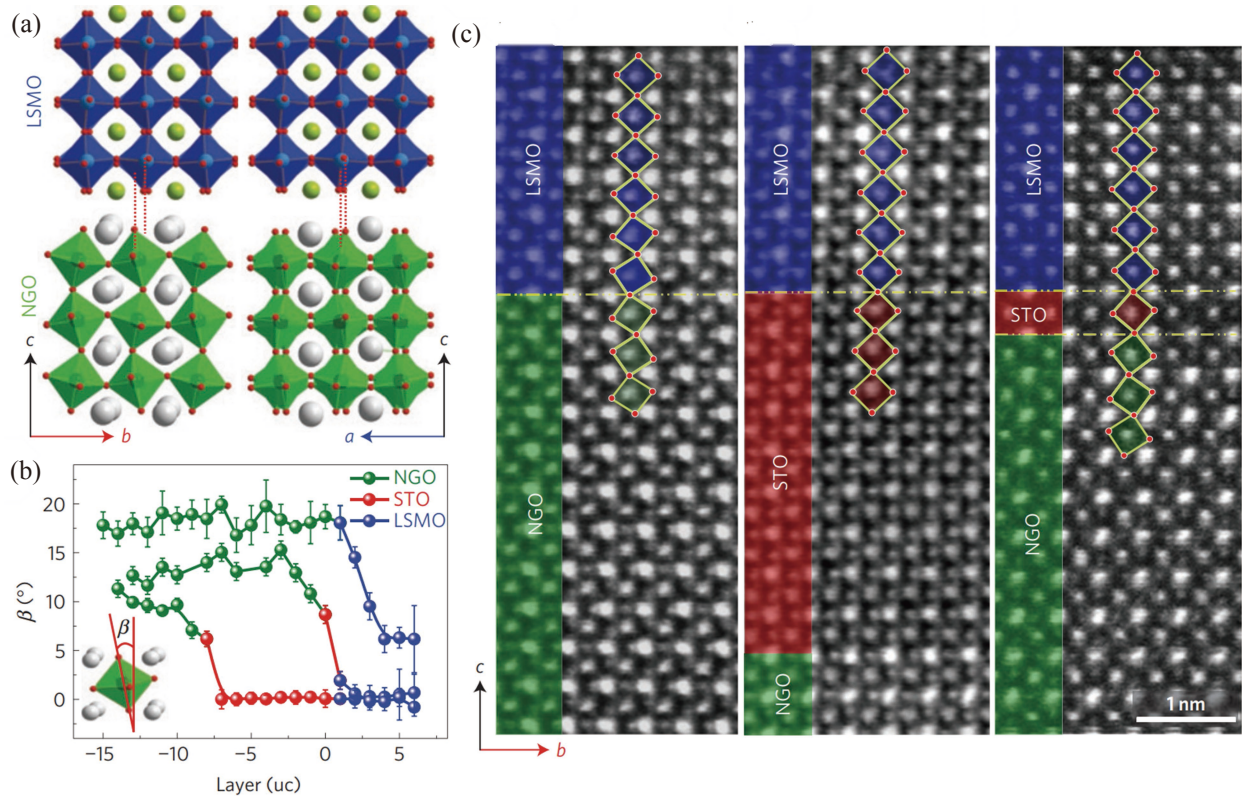
Fig. 2. Oxygen octahedral coupling at the heterointerface between perovskite oxides. (a) Schematic diagram of octahedral rotation in LSMO and NGO interface. (b) Layer-position-dependent mean octahedral tilt angle (β) in LSMO/NGO heterostructures with and without a STO buffer layer. The data for the non-buffered sample are shifted upwards by 6° for clarity. (c) It shows ABF-STEM images of LSMO/NGO, LSMO/STO$_9$/NGO and LSMO/STO$_1$/NGO heterostructures. Figure taken from Ref. [33].

Fig. 3a, peaks (103) and (−103) show symmetric diffraction patterns for axes a and c with orthogonality preserved. In contrast, an asymmetric counterpart was shown due to the destroyed orthogonality between the b and c axes. More importantly, in the La$_{2/3}$Sr$_{1/3}$MnO$_3$ (LSMO)/PbTiO$_3$(PTO)/LSMO/(110) NGO heterostructure, the RSM can identify different octahedral rotations for each LSMO layer, unraveling the appearance of multiple Curie temperatures and coercive fields. The schematic diagrams of different heterostructures and the corresponding HO-XRD spectra are shown in Fig. 3b and 3c.

Compared with Fig. 3c, the origin of the weak and wide blue diffraction peaks in Fig. 3b cannot be identified. At this point, the RSM based on the cation lattice showed its unique advantages in matching these diffraction peaks to the corresponding layer. Fig. 3d resents the RSM patterns around different crystal planes. The LSMO-1 layer with a larger L reveals symmetric (±103) diffraction peaks and asymmetrical (0±13) diffraction peaks, thus revealing the monoclinic ion lattice (i.e., $\alpha \neq 90, \beta = \gamma = 90$) and the "+ − −" rotation mode. The RSM pattern of the LSMO-2 layer (see the orange arrows) was observed at a lower L index, showing symmetric (±103) and (0 ±13) peaks, thus it has a "000" mode with $\alpha = \beta = \gamma = 90°$ in the cationic lattice. In addition, the PTO layer (indicated by dotted green lines) has symmetric (±103) and (0 ±13) diffraction patterns, indicating that the "000" mode of the bulk is preserved in the film. In conclusion, RSM is used to achieve the qualitative characterization of the octahedral rotation mode of the (LSMO)$_9$/(PTO)$_{12}$/(LSMO)$_9$/(110)NGO heterostructure based on the correlation between the cationic lattice and octahedral rotation mode, which provides a new research method for OOR in complex multilayer heterostructures.

STEM is still the mainstream means to characterize the OOR due to its extremely intuitive and quantifiable experimental results[32, 33, 40, 43]. Fig. 2c shows the high-resolution ABF-STEM image at the LSMO/STO/(110)NGO heterointerface[33], which exhibits the in-phase rotation of the [GaO$_6$] octahedra around the a-axis direction. In addition, detecting the OOR globally is appropriate by changing the slicing direction of the sample[32, 44]. Here, the ABF results show that the LSMO films exhibit an in-phase OOR mode at the interface, consistent with the [GaO$_6$] octahedra in the NGO substrate. The rotational amplitude exhibits a continuous attenuation from the interface to the interior of the film, disappearing rapidly when the thickness is greater than 4 unit cells (u.c.) Interestingly, inserting a nonrotated (a^{0}a^{0}a^0) STO layer in the LSMO/NGO heterostructure made the OOR amplitude decay rapidly and disappear after 2 u.c. (as shown in the middle panel of Fig. 2c). Using STEM to detect interfacial structures, one can "patch" the clear outline of the oxygen octahedra.

In general, HO-XRD and STEM, as two techniques to characterize OOR, have received extensive attention due to their intuitive measurement results. However, these methods still have some limitations. For example, HO-XRD can only reflect the global OOR without spatial resolution, and a direct measurement of OOR requires highly sophisticated experimental techniques, such as the synchrotron light source. On the other hand, the aberration corrector should be equipped in
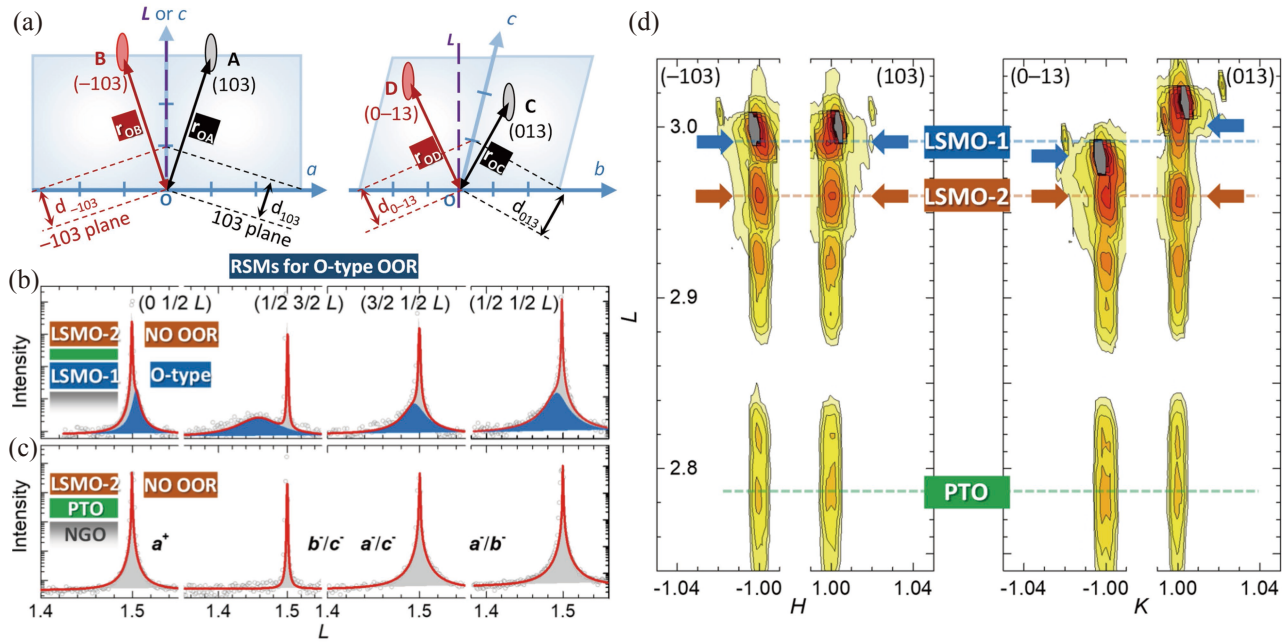
Fig. 3. RSM characterization of oxygen octahedral rotation. (a) The sketches of the RSM with symmetric and asymmetric reflections, where r_{OA}, r_{OB}, r_{OC} and r_{OD} represent reciprocal vectors. (b) and (c) display different half-order X-ray diffraction spectrum corresponding to the heterostructures, and the blue part in (b) is obtained by peak fitting. (d) The RSMs of LSMO/PTO/LSMO/NGO along different diffraction faces. Figure taken from Ref. [42].

STEM to improve the imaging resolution. Therefore, it is necessary to develop new technologies (such as RSM here) for determining octahedral rotation[42]. In addition, other characterization techniques, including extended X-ray absorption fine structure spectroscopy (EXAFS)[45–49], coherent Bragg diffraction rod analysis (CBRA)[50, 51], Raman scattering spectroscopy[5, 6, 52–54], also play an important role in the direct or indirect OOR measurement.

3   Tailoring properties by octahedral rotation

3.1   Octahedral distortion

Chemical doping or external stress can lead to the distortion of the [BO₆] octahedra in perovskite oxides, including size distortion and shape distortion, thereby affecting properties. The distortion that the B–O–B bond angle remains constant and the B–O bond length increases or decreases by the same degree is called size-distortion (Q1 mode), also known as the "breathing effect" of the octahedra. This will cause a network with the same octahedra shape but different sizes, which can induce charge disproportionation of B-site ions through the B–O electrostatic interaction, thereby forming a new B-site ion valence state and charge order[55–58], giving rise to many novel phenomena, such as Mott insulator[59, 60], metal-insulator transition[61, 62], ferroelectricity[63, 64], and ferromagnetism[55]. Another type of octahedral distortion, known as shape distortion, is characterized by the fact that the B–O–B bond angles do not change significantly, but the bond lengths no longer remain constant. Generally, the change in bond lengths for in-plane and out-of-plane have opposite trends, which are called the Q₂ mode or Q₃ mode, also known as the Jahn-Teller distortion. Shape distortion can induce the polarization of the B-site d orbital through the electron phonon interaction, lifting the degeneracy of the e_g orbital or the t_{2g} orbital to form an or-

bital order, which is very common in 3d manganese oxides[65–67]. In addition, perovskite oxides composed of transition metal elements with d^0 electrons (such as Ti^{4+}) or main-group elements with $6s^2$ electrons (such as Pb and Bi) will spontaneously generate ferroelectric polarization due to the broken inversion symmetry, which is also classified as an octahedral shape distortion[68, 69].

3.2   Octahedral rotation

Lattice size and symmetry match are two factors that need to be considered first during film epitaxy. To maintain a continuous three-dimensional oxygen octahedra structure at the heterointerface, the substrate needs to impose geometric constraints on the oxide film, thereby affecting the rotation amplitude of the octahedra. In fact, the symmetry induced by the octahedral coupling can penetrate the entire epitaxial film if the growth fashion of coherent epitaxy is maintained[70]. Recently, interesting physical phenomena, such as the metal-insulator transition, antiferromagnetic-paramagnetic phase transitions, and polar metal states modulated by [NiO₆] octahedral rotation, have been reported in nickelate superlattices[40, 71–73]. Controllable modulation of the magnetization, anisotropy and other properties can also be achieved by tailoring the OOR mode and amplitude[16, 33, 74, 75]. Expectedly, the B–O–B bond angle change caused by the OOR can significantly enhance the Dzyaloshinskii-Moriya interaction (DMI) due to broken inversion symmetry, thereby leading to a topological Hall effect[76–78]. In addition, the presence of the OOR in paraelectric oxides can also lead to metastable ferroelectric order and complex electrical polarization states[39, 79, 80].

3.2.1   Modulating electrical properties

3.2.1.1   Metal-insulator transition
The basic electric transition of the simplest correlated electronic system is jointly characterized by the Coulomb repulsion potential and electronic hopping term, where the d elec-

tron hopping between two B-sites is mediated by the O 2p orbital. OOR changes the B–O–B bond angle, which tailors the overlap integral between the d orbital and O 2p orbital[81]. Specifically, when the bond angle of B–O–B deviates from 180°, the hopping constant decreases and the d electron band becomes narrow. A larger tilt usually induces a narrower band width, so eventually, a gap is opened around the Fermi level and the metal-insulator transition (MIT) occurs. The MIT behavior[40, 72, 73, 82] has been tuned preciously by constructing artificial superlattices to control the rotation modes and amplitudes, which has been widely studied in nickelate oxides.

Tunable transport behavior and magnetism ground state were reported in a rare-earth nickelate SmNiO$_3$(SNO) by controlling the OOR[72], where LaFeO$_3$(LFO), LaCrO$_3$(LCO), and LaNiO$_3$(LNO) with identical symmetry and different tilt magnitudes were used as templates. Fig. 4a shows the tunable conductance and metal-insulator transition temperature T_{MIT} with varying thickness (n) of the SNO layer in different LFO$_1$-SNO$_n$ (n = 4–10) superlattices. In particular, the T_{MIT} of the LFO$_1$-SNO$_4$ superlattice is only 78 K, which is much lower than that of SNO$_{30}$ (356 K). As the thickness of the SNO layer increases, the structural modulation effect of the LFO$_1$ layer becomes weaker, driving T_{MIT} toward higher temperatures and then approaching that of the SNO$_{30}$ film. X-ray absorption spectroscopy (XAS) of the Ni-L$_{2,3}$ edge illustrated the intrinsic mechanism of T_{MIT} (Fig. 4d). The splitting of the Ni L edge is suggested to depend on both the magnitude of the breathing mode distortion and the size of the Ni–O–Ni hopping interaction. A smaller splitting energy indicates a

smaller Ni–O–Ni interaction and a smaller breathing distortion. On the other hand, as shown in Fig. 4b, SNO$_4$-based superlattices constructed with different tilt templates, LCO and LNO, also exhibited lower T_{MIT} than SNO$_{30}$. Interestingly, the LNO bulk has a smaller octahedral tilt (5.3°) than LFO (6.8°), while LNO$_1$-SNO$_4$ exhibits higher T_{MIT} than LFO$_1$-SNO$_4$. This is because LNO is subjected to a tensile stress, resulting in a smaller out-of-plane lattice and a larger rotation amplitude of octahedra. In contrast, LFO is under compressive stress, so the [NiO$_6$] tilt angle will decrease. Furthermore, the Néel temperatures T_N of different superlattices are observed to be positively correlated with T_{MIT} by resonant magnetic diffraction (RMD), as shown in Fig. 4c. These results demonstrated the remote control of the ground state properties of nickelates through interfacial OOR modulation. The phase diagram shown in Fig. 4e reveals the correlation between the microscope structure and the physical states, which supplies new perspectives for the controllable design of novel quantum materials. Similarly, Chen et al.[40] observed tunable metal-insulator transition and antiferromagnetic-paramagnetic transition behaviors in NdNiO$_3$/SrTiO$_3$ superlattices by changing the thickness of NdNiO$_3$. In addition, ionic liquid gating is also an effective method to modulate the octahedra rotation, as reported by Liu et al.[82] in WO$_3$ films. Dong et al.[73] observed an almost zero thermal hysteresis effect at T_{MIT} in a NdNiO$_3$/NGO heterostructure by reducing the Ni–O–Ni bond angle through interface octahedral coupling. Notably, the d-orbital polarization induced by octahedral rotation may give rise to MIT, which plays a significant role similar to the
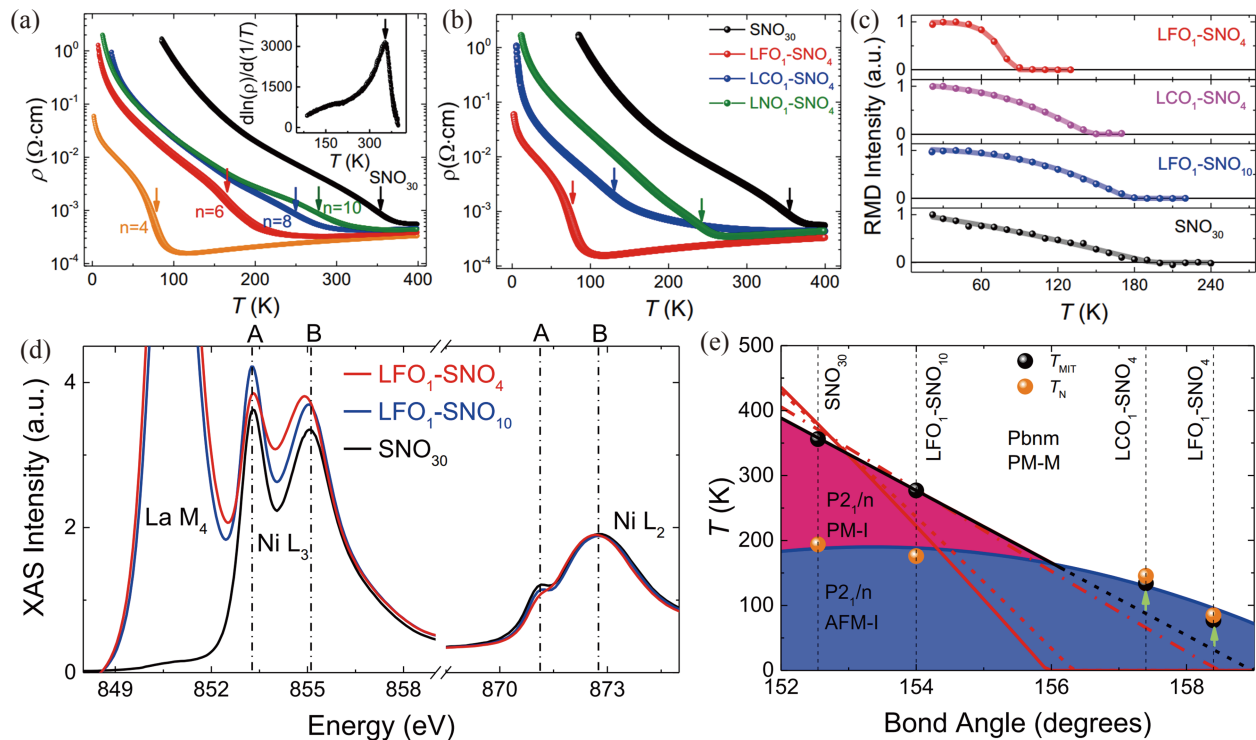

Fig. 4. MIT in nickelate superlattices triggered by oxygen octahedral coupling. (a) ρ-T curves of LFO$_{-1}$-SNO$_n$ (n = 4–10) superlattices and 30 u.c. SNO film, and the inset shows the first derivative dlnp/(d(1/T)) of the SNO$_{30}$ film. (b) ρ-T curves of SNO$_4$ superlattices constructing with LFO, LCO and LNO. (c) Temperature dependent intensity of (1/4, 1/4, 1/4) magnetic Bragg reflection peak. (d) X-ray absorption spectra (XAS) of Ni L$_{2,3}$ edge of nickelate superlattices with different thicknesses at 22 K. (e) Temperature phase diagram of nickelate superlattices as a function of the mean Ni–O–Ni bond angle. Figure taken from Ref. [72].

OOR amplitude[83], providing a new theoretical basis for tuning physical properties.

3.2.1.2 Magnetic transport modulation

Double exchange and the Stoner model are the two most important theories for understanding the ferromagnetism in oxides[84, 85]. Typical ferromagnetic oxides, 3d manganate and 4d ruthenate, have a finite electronic density of states at the Fermi level, revealing good metallic behavior. These perovskite oxides possess fascinating properties, such as a giant magnetoresistance effect, anomalous Hall effect, and topological Hall effect[62, 76, 77, 86], which can be tuned and modified by manipulating the delicate coupling of spin, orbit, charge, and lattice.

As a lattice-level modulation strategy, interfacial OOR coupling has attracted much attention in electro and magnet transport in recent years. Zhang et al.[86] realized the low-temperature irreversible magnetoresistance effect in $Pr_{0.67}Sr_{0.33}MnO_3$ through OOR amplitude modulation at the substrate-film heterointerface. The topological Hall effect (THE) is a significant transport feature of chiral spin textures in real space, such as skyrmions[87, 88]. Ziese et al.[76] prepared $SrRuO_3/Pr_{0.7}Ca_{0.3}MnO_3$ (PCMO) superlattices to explore the origin of the THE in SRO/FMO (ferromagnetic oxide) systems. Interestingly, their study pointed out that PCMO can induce the [RuO_6] OOR in the interfacial layer, resulting in different symmetry from the bulk. As is known, the magnitude and sign of anomalous Hall resistance are closely related to lattice structure; thus, the global contribution from multichannel anomalous Hall signals with opposite signs can imitate anomalous Hall signals with topological characteristics. Qin et al.[77] observed the THE in single SRO films less than 10 nm, pointing out that a heavy metal oxide capping layer (such as $SrIrO_3$) is not necessary for the topological Hall signal. Additionally, the temperature and magnetic field windows for THE can be tuned by changing the oxygen partial pressure, which is attributed to [RuO_6] octahedral rotation.

Not just OOR, however, structural phases transition, defects[15, 89], and multiple rotation modes at the heterointerface can also be induced by varying oxygen partial pressure, so OOR is just a handwaving origin of the THE here. In view of this, Gu et al.[78] prepared $SRO_M/STO(001)$ (where $M = 5$–10 u.c.) and $SRO_8/BTO_N/STO(001)$ (where $N = 2$–4 u.c.) heterojunctions to clarify the correlation between THE and OOR. Fig. 5a shows the geometric analysis of interfacial oxygen octahedra. The transport results showed that THE can be observed in the $SRO_M/STO(001)$ heterostructure with $M < 10$ u.c., especially in the sample $SRO_8/STO(001)$ with $M = 8$ u.c. (see Fig. 5b, left). As a comparison, the counterparts buffered by N u.c. $BaTiO_3$(BTO) were prepared. Interestingly, the THE completely disappeared when $N > 2$ u.c., while a weak THE was reproduced in the heterojunction with $N = 2$ u.c. (Fig. 5b, right). HAADF-STEM and ABF-STEM were further utilized to analyze the OOR. As shown in Fig. 5a, the [RuO_6] octahedra at the $SRO_8/STO(001)$ heterointerface have an OOR angle of ~3° and decay rapidly away from the interface. Obviously, the symmetry difference between the interface and inside leads to inversion symmetry breaking near the interface, which effectively increases the DMI, thus enhancing the topological Hall signal. Additionally, the OOR was

effectively suppressed by inserting buffer layer BTO with larger radius A-site ions, so it showed a decreased topological Hall signal. In addition to interfacial bonding, Lin et al.[90] demonstrated tunable OOR by switching the structure of the proximity layer (planar ↔ chain) utilizing the thickness sensitivity of the $SrCuO_2$ (SCO) geometry. By constructing SCO/SRO/SCO sandwiches with different SCO thicknesses, two different OOR modes of [RuO_6] octahedra were realized at the interfaces, resulting in the spin state changes of Ru at the interfaces as well as the hybrid of Ru 4d and O 2p, thereby greatly modulating the magnetic resistance and anomalous Hall resistance.

3.2.1.3 Electric polarization modulation

Symmetry propagation induced by the OOR has demonstrated many strong impacts on the transport behavior of complex oxide films as mentioned above. The highly insulating prototypical ferroelectric oxides, however, typically for $BaTiO_3$ and $PbTiO_3$, have no octahedral rotations. On the other hand, perovskites with OOR can exhibit conductance but are not polar or ferroelectric. This fact seems to imply incompatibility between the OOR and ferroelectric polarization. However, Kim et al.[79] found [TiO_6] octahedral rotation-related metastable room temperature ferroelectricity in $CaTiO_3$ by interfacing with a $LaAlO_3$ layer, which was further verified by DFT calculations. Similarly, Pramanick et al.[91] realized OOR mode ordering ($a^-a^-a^-$) by applying an electric field to the 200 nm thick polycrystalline ferroelectric $Na_{1/2}Bi_{1/2}TiO_3$(NBT). The two examples have already shown the fact that OOR and ferroelectric polarization coexist. Benedek et al.[92] pointed out that the OOR itself generally does not quench B-site ion ferroelectric polarization, but the accompanying A-site anti-polar displacements can play a crucial role in suppressing the ferroelectricity in *Pnma* or other space groups that allow rotation distortions. When A-site distortion is absent, many perovskites would adopt the *R3c* space group, which is allowed to exhibit ferroelectricity.

Interestingly, an electric polarization rotation pattern, a novel emergent ferroelectric structure induced by interfacial OOR coupling, was observed in the PTO/STO heterojunction[39]. HAADF-STEM clearly demonstrates the rotating electric polarization in PTO, as shown in Fig. 6a. Generally, many different polarization modes can be evolved in PTO films due to the depolarization field. However, it can be ruled out by the counterpart, the Nb:STO substrate with good conductivity. Furthermore, the authors used ABF-STEM to reveal the displacement δ_{Ti-O} of Ti^{4+} in both the in-plane and out-of-plane directions (Fig. 6b and 6c). The displacement orientation varies with thickness, thus exhibiting rotational electric polarization in the PTO. Their DFT calculations (see Fig. 6d), as well as earlier theoretical predictions[36], indicated that the rotational electric polarization is related to the antiferroelectric distortion (AFD) caused by in- and out-of-plane OOR. The ferroelectric PTO without AFD (Model A) showed normal polarization, while that with AFD (Model B) showed a rotational pattern. In addition to electric polarization modulation, Geng et al.[93] also observed a ferroelectric-antiferroelectric phase transition mediated by OOR coupling in an ultrathin $BiFeO_3$ system.
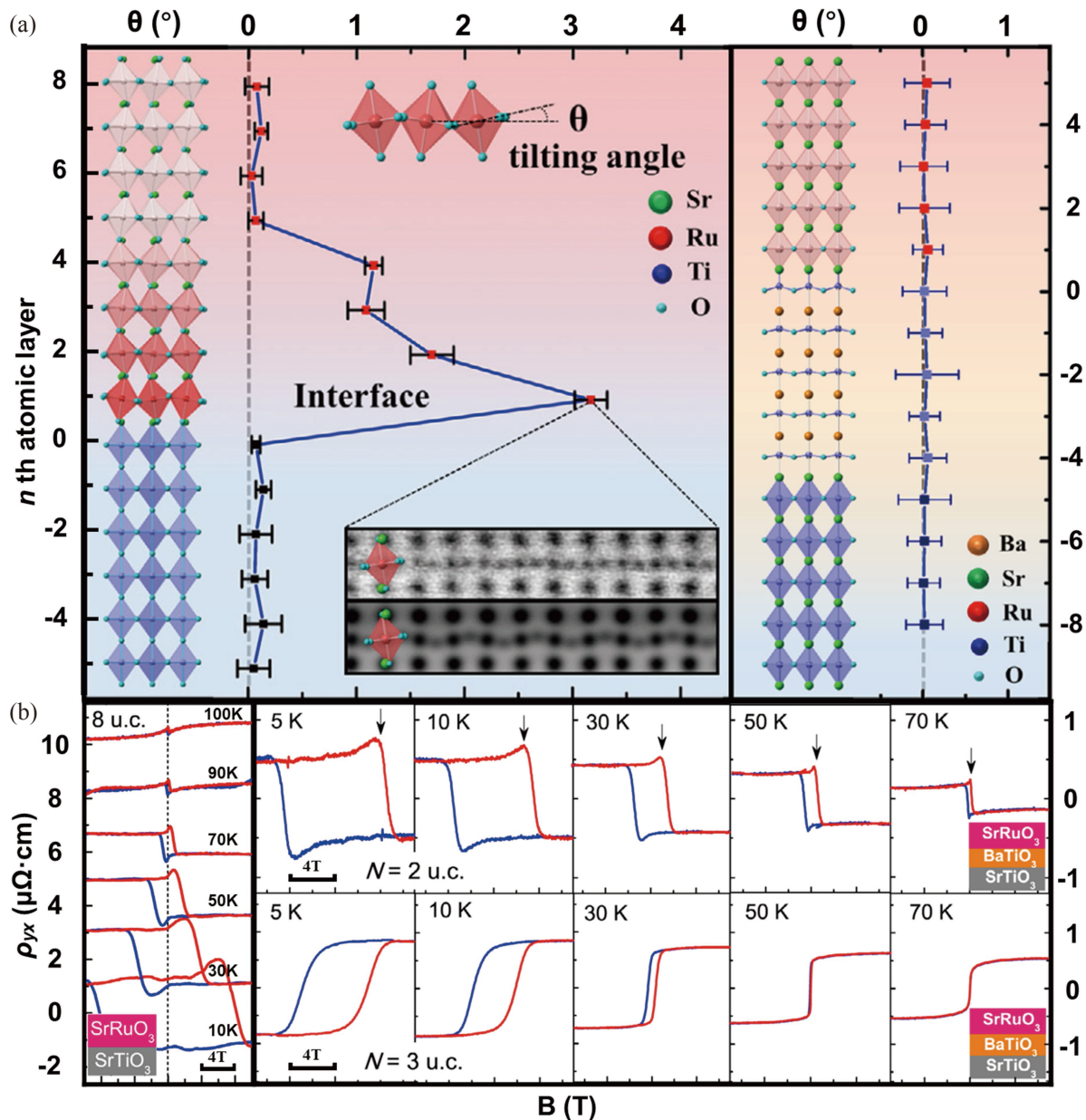
Fig. 5. Octahedral rotation tailoring topological Hall effect. (a) The left figure shows the sketch of the octahedra configuration at the SRO/STO hetero-interface and the statistical results of rotation angle, and the inset respectively show the [RuO$_6$] octahedral-rotation ABF image at the first layer of the interface and the simulation results. The figure on the right of the panel shows the statistics result of the rotation angle of the octahedron after inserting the 4 u.c. BTO. (b) The left picture shows the anomalous Hall resistance (AHR) of SRO (8 u.c.)/STO heterostructure at different temperatures, and the right one shows the AHR curve of SRO$_8$/BTO$_N$ ($N = 2$, 3)/STO at varying temperatures. Figure taken from Ref. [78].

3.2.2 Modulating magnetism

Manganate, cobaltate and ruthenate are the three most studied magnetic perovskites. The exchange interaction stiffness J, characterized by the Curie temperature ($J \sim 3/2K_BT_C$), can be tuned by manipulating the oxygen octahedral rotation[94]. In addition, the OOR can cause the orbital occupation of B-site ions to realize the modulation of magnetic anisotropy[95]. The magnetic easy axis switching of LSMO films grown on NGO substrates can be achieved by inserting a nonrotating STO ($a^0a^0a^0$) buffer layer[33]. As shown in Fig. 7a, the easy axis of the nonbuffered LSMO is the *a*-axis, in strong contrast to the observed *b*-axis easy axis in the thick one. By inserting the STO buffer layer, the easy axis of the LSMO can be switched

to the *b*-axis again. Fig. 7b and 7c demonstrate the easy axis switching of LSMO films after being buffered by 1 u.c. and 9 u.c. STO buffer layers, respectively. To further determine the magnetization distribution of Mn, resonant X-ray reflection (RXR) was used to probe the magnetic profile of LSMO (6 u.c.) film without the STO buffer layer and that with 9 u.c. STO buffer layer (Fig. 7d). The spatial distribution of Ga, Ti, and Mn atoms demonstrates the atomic-level flat heterointerface. The decay length of octahedral rotation here is 2 nm, so it still exists on the surface of the LSMO film with a thickness of 6 u.c. Compared with the LSMO film without a buffer layer, the one buffered by STO has a smaller OOR (see Fig. 7d), thus exhibiting a more uniform magnetic profile and
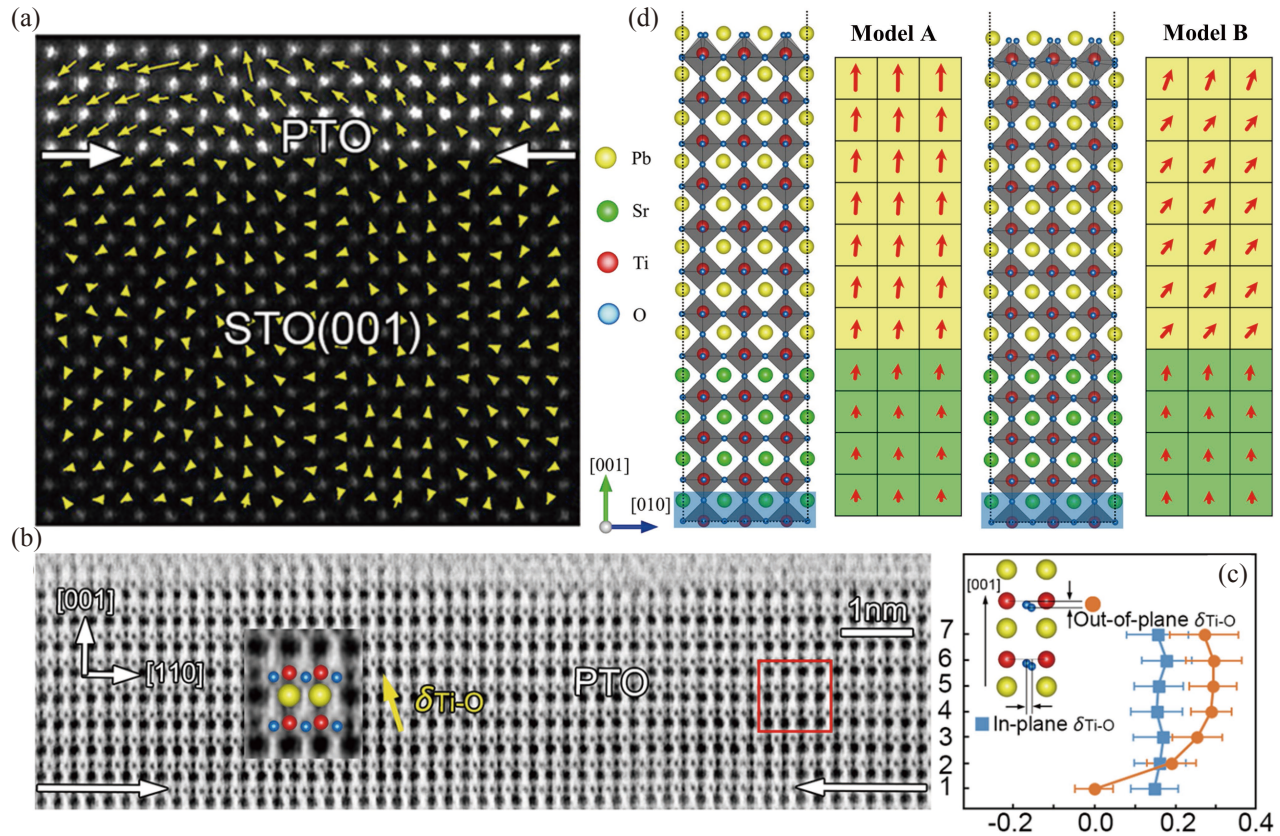
Fig. 6. Rotation of electric polarization induced by oxygen octahedral rotation. (a) HAADF-STEM image of the 1.6 nm thick PTO film and the electric polarization distribution. (b) are the ABF-STEM results. (c) Magnitude (δ_{Ti-O}) of Ti^{4+} deviated from the oxygen octahedra center in- and out-of- plane of the 3.2 nm PTO film, respectively. (d) First-principles calculation results, where Model A and Model B give the relaxed atomic configuration with and without AFD, respectively. And the results of the electrical polarization simulation are shown on the right. Figure taken from Ref. [39].

a smaller thickness of the surface magnetic dead layer. This result in turn explains the enhanced saturation magnetization exhibited in Fig. 7b and 7c. The different saturation magnetization and magnetic anisotropy switching caused by the inserted STO buffer layer can be attributed to the difference in the hybridization strength between O 2p and Mn 3d caused by different OOR modes and amplitudes[94].

Meanwhile, Kan et al.[16] discovered the modulation of magnetic anisotropy mediated by OOR in the SRO/$Ca_{0.5}Sr_{0.5}TiO_3$/GaScO$_3$ heterostructure, and realized the switching of the magnetic easy axis of SRO. Subsequently, Zhang et al.[96] constructed an LSMO/LaCoO$_{2.5}$ interface with a large symmetry mismatch, and strong perpendicular magnetic anisotropy was observed. Meng et al.[97] observed the suppressed [RuO$_6$] octahedral rotation caused by proximity [TiO$_6$] octahedral couple at the interface of the BTO/SRO/BTO heterostructure. Enhanced ferromagnetism and metallicity as well as Ru^{4+} displacement polarization in the sandwich were demonstrated by STEM, transport and magnetic characterization, demonstrating the coexistence of ferromagnetism-metal-polarization tristate in the SRO layer.

4   Summary and perspective

The physical properties of ABO$_3$ perovskite oxides are strongly related to the structure of the oxygen octahedral network, and the controllable design can be achieved by adjusting the size and shape of the [BO$_6$] octahedral unit, as well as

the OOR mode and amplitude. At present, there are two common methods to control the OOR mode: interfacial strain engineering and symmetry mismatch coupling. For the former, the additional strain effect, not just OOR, has a manifesting contribution to tailor the properties as well. The latter, i.e., interface octahedral coupling, it has received much attention in recent years. The OOR can affect physical properties from two aspects. On the one hand, emergent physical properties can be generated by intertwining with the charge, spin, and orbital degrees of freedom; on the other hand, its original physical properties, such as magnetization or electric polarization, can be enhanced or improved to an unexpected level.

Benefiting from the rapid development of thin film growth technology, artificial oxide materials with complex interfacial structures and different lattice symmetries can be prepared. Conducting atomic-level analysis using techniques such as STEM can be a route to understand the key relationship between OOR and material processing. Importantly, designing the OOR at the atomic level is a controllable strategy to locate many functional oxides to phase boundaries, so as to capture obvious and emergent functional responses induced by external fields (electric, magnetic, and stress fields). In this paper, several typical examples, including, controlled electro- and magneto- transport, electrical polarization, and magnetism are presented. However, to develop and realize device applications utilizing the OOR effect, it is crucial to understand the following fundamental issues: How can the
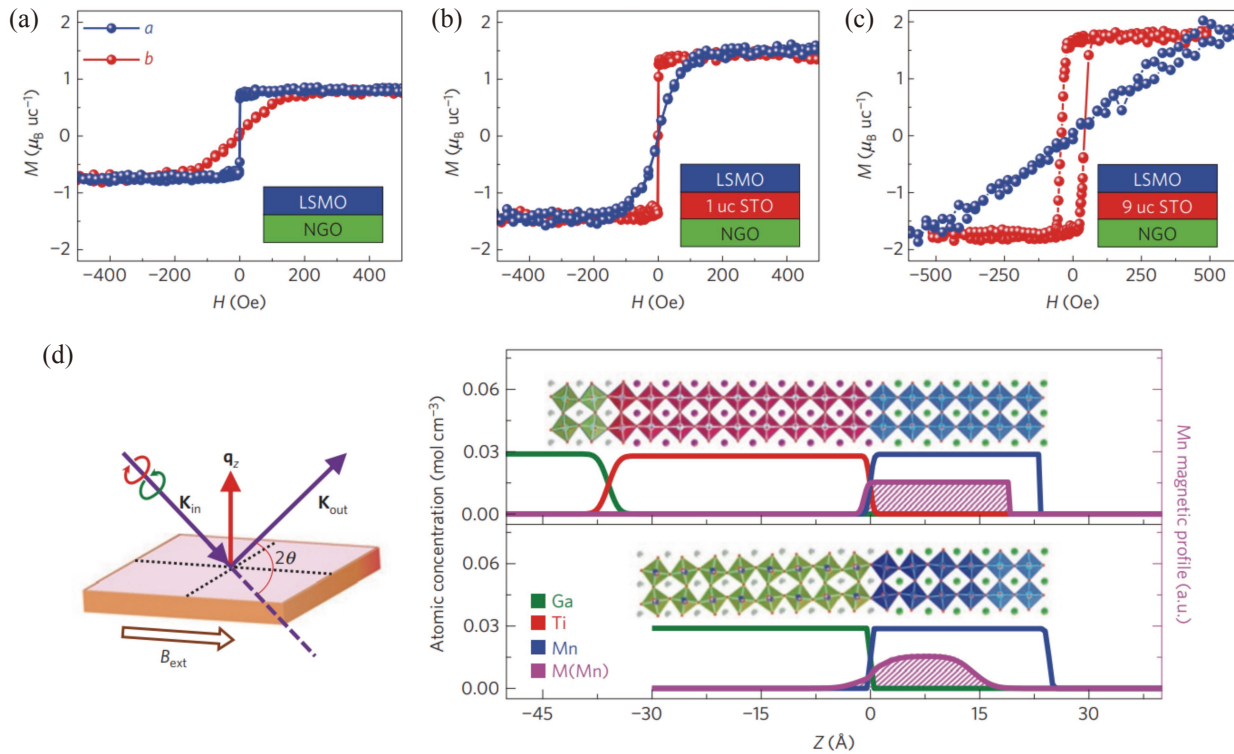
Fig. 7. Magnetic anisotropy in the magnetic heterojunctions. (a)–(c) show the M-H curves of the LSMO film along the *a*-axis and *b*-axis of the NGO substrate, where (a), (b), and (c) show the results of inserting 0 u.c., 1 u.c., and 9 u.c. STO buffer layers, respectively. (d) RXR measurements of 6 u.c. LSMO films with (top panel) and without (bottom panel) a 9 u.c. STO buffer layer showing depth profiles of the Ga, Ti, and Mn atomic concentration (green, red, and blue lines, respectively) and Mn magnetization (M, purple line with shaded area) at 20 K. The schematic on the left shows the experimental set-up used to perform RXR measurements, where a 0.6 T magnetic field was applied in-plane along the magnetic easy axis during the measurement. Figure taken from Ref. [33].

OOR be quantitatively predicted and described in thin films at heterointerfaces with arbitrary symmetry mismatch? What are the key parameters and mechanisms that determine the relaxation length of OOR coupling? Is it possible to independently manipulate the octahedral behavior along the in-plane and out-of-plane directions? Resolving these key issues is beneficial to further understand the OOR behavior and predict the physical properties of materials. Through subtle design, the functional properties of complex oxide heterostructures and devices can be tuned and developed.

Acknowledgements

Conflict of interest

The authors declare that they have no conflict of interest.

Biographies

Junhua Liu is currently a Ph.D. student, and his research interests focus on emergent phenomena of transition metal oxides interface.

Zhaoliang Liao is a Professor at the University of Science and Technology of China. He received his Ph.D. degree from the Institute of Physics, CAS and Louisiana State University. He is supported by the Hundred-Talent Program Funding CAS and Youth Funding of Chinese National Innovative Talents Program. He focuses on the preparation and character-

ization of epitaxial quantum functional thin film materials and is committed to the design and function tailoring of oxides heterostructure utilizing advanced epitaxial growth technology. He has published several papers in high-level international journals, including *Nat. Mater.*, *Nat. Commun.*, *PNAS*, *Nano Lett.*, *PRL*, *Adv. Funct. Mater.*, *Adv. Mater.*, and *Sci. Adv.*.

References

[1] Hassenzahl W V, Hazelton D W, Johnson B K, et al. Electric power applications of superconductivity. *Proceedings of the IEEE,* **2004**, *92* (10): 1655–1674.

[2] Daughton J, Chen Y. GMR materials for low field applications. *IEEE Transactions on Magnetics,* **1993**, *29* (6): 2705–2710.

[3] Wang W, Tadé M O, Shao Z. Research progress of perovskite materials in photocatalysis- and photovoltaics-related energy conversion and environmental treatment. *Chemical Society Reviews,* **2015**, *44* (15): 5371–5408.

[4] Imada M, Fujimori A, Tokura Y. Metal-insulator transitions. *Reviews of Modern Physics,* **1998**, *70* (4): 1039.

[5] Schober A, Fowlie J, Guennou M, et al. Vibrational properties of LaNiO₃ films in the ultrathin regime. *APL Materials,* **2020**, *8* (6): 061102.

[6] Raj A, Kumar M, Mishra D, et al. Raman and photoluminescence spectral studies in epitaxial Bi₂NiMnO₆ double perovskite thin-film samples. *Optical Materials,* **2020**, *101*: 109773.

[7] Glazer A. Simple ways of determining perovskite structures. *Acta Crystallographica, Section A: Crystal Physics, Diffraction, Theoretical and General Crystallography,* **1975**, *31* (6): 756–762.

[8] Ohtomo A, Hwang H. A high-mobility electron gas at the LaAlO₃/SrTiO₃ heterointerface. *Nature,* **2004**, *427* (6973): 423–426.

[9] Reyren N, Thiel S, Caviglia A, et al. Superconducting interfaces between insulating oxides. *Science,* **2007**, *317* (5842): 1196–1199.

[10] Brinkman A, Huijben M, Van Zalk M, et al. Magnetic effects at the

interface between non-magnetic oxides. *Nature Materials,* **2007**, *6* (7): 493–496.

[11] Takahashi K, Kawasaki M, Tokura Y. Interface ferromagnetism in oxide superlattices of $CaMnO_3/CaRuO_3$. *Applied Physics Letters,* **2001**, *79* (9): 1324–1326.

[12] He J, Borisevich A, Kalinin S V, et al. Control of octahedral tilts and magnetic properties of perovskite oxide heterostructures by substrate symmetry. *Physical Review Letters,* **2010**, *105* (22): 227203.

[13] Lee S S, Kim Y M, Lee H J, et al. Correlation between geometrically induced oxygen octahedral tilts and multiferroic behaviors in $BiFeO_3$ films. *Advanced Functional Materials,* **2018**, *28* (19): 1800839.

[14] Thomas S, Kuiper B, Hu J, et al. Localized control of Curie temperature in perovskite oxide film by capping-layer-induced octahedral distortion. *Physical Review Letters,* **2017**, *119* (17): 177203.

[15] Lu W, Yang P, Song W D, et al. Control of oxygen octahedral rotations and physical properties in $SrRuO_3$ films. *Physical Review B,* **2013**, *88* (21): 214115.

[16] Kan D, Aso R, Sato R, et al. Tuning magnetic anisotropy by interfacially engineering the oxygen coordination environment in a transition metal oxide. *Nature Materials,* **2016**, *15* (4): 432–437.

[17] Gao R, Dong Y Q, Xu H, et al. Interfacial octahedral rotation mismatch control of the symmetry and properties of $SrRuO_3$. *ACS Applied Materials & Interfaces,* **2016**, *8* (23): 14871–14878.

[18] Jaramillo R, Ha S D, Silevitch D M, et al. Origins of bad-metal conductivity and the insulator-metal transition in the rare-earth nickelates. *Nature Physics,* **2014**, *10* (4): 304–307.

[19] Rondinelli J M, Fennie C J. Octahedral rotation-induced ferroelectricity in cation ordered perovskites. *Advanced Materials,* **2012**, *24* (15): 1961–1968.

[20] Benedek N A, Mulder A T, Fennie C J. Polar octahedral rotations: A path to new multifunctional materials. *Journal of Solid State Chemistry,* **2012**, *195*: 11–20.

[21] Cui Y, Liu X, Fan W, et al. Metal–insulator transition in $RNiO_3$ (R = Pr, Nd, Sm, Gd, Tb, Dy, Ho, Er) induced by Li doping: A first-principles study. *Journal of Applied Physics,* **2021**, *129* (23): 235107.

[22] Mercy A, Bieder J, Íñiguez J, et al. Structurally triggered metal-insulator transition in rare-earth nickelates. *Nature Communications,* **2017**, *8* (1): 1677.

[23] Subedi A, Peil O E, Georges A. Low-energy description of the metal-insulator transition in the rare-earth nickelates. *Physical Review B,* **2015**, *91* (7): 075128.

[24] Goldschmidt V M. Die gesetze der krystallochemie. *Naturwissenschaften,* **1926**, *14* (21): 477–485.

[25] Filip M R, Giustino F. The geometric blueprint of perovskites. *Proceedings of the National Academy of Sciences of the United States of America,* **2018**, *115* (21): 5397–5402.

[26] Bartel C J, Sutton C, Goldsmith B R, et al. New tolerance factor to predict the stability of perovskite oxides and halides. *Science Advances,* **2019**, *5* (2): eaav0693.

[27] Woodward D I, Reaney I M. Electron diffraction of tilted perovskites. *Acta Crystallographica Section B:Structural Science,* **2005**, *61*: 387–399.

[28] Jia C L, Mi S B, Faley M, et al. Oxygen octahedron reconstruction in the $SrTiO_3/LaAlO_3$ heterointerfaces investigated using aberration-corrected ultrahigh-resolution transmission electron microscopy. *Physical Review B,* **2009**, *79* (8): 081405.

[29] May S J, Kim J W, Rondinelli J M, et al. Quantifying octahedral rotations in strained perovskite oxide films. *Physical Review B,* **2010**, *82* (1): 014110.

[30] Glazer A. The classification of tilted octahedra in perovskites. *Acta Crystallographica, Section B: Structural Crystallography and Crystal Chemistry,* **1972**, *28* (11): 3384–3392.

[31] Liao Z, Green R J, Gauquelin N, et al. Long–range domain structure and symmetry engineering by interfacial oxygen octahedral coupling at heterostructure interface. *Advanced Functional Materials,* **2016**, *26* (36): 6627–6634.

[32] Aso R, Kan D, Shimakawa Y, et al. Atomic level observation of

octahedral distortions at the perovskite oxide heterointerface. *Scientific Reports,* **2013**, *3*: 2214.

[33] Liao Z, Huijben M, Zhong Z, et al. Controlled lateral anisotropy in correlated manganite heterostructures by interface-engineered oxygen octahedral coupling. *Nature Materials,* **2016**, *15* (4): 425–431.

[34] Samanta K, Ležaić M, Blügel S, et al. Tailoring the anomalous Hall effect of $SrRuO_3$ thin films by strain: A first principles study. *Journal of Applied Physics,* **2021**, *129* (9): 093904.

[35] Wang L, Pan W, Han D, et al. First-principles calculations of oxygen octahedral distortions in $LaAlO_3/SrTiO_3$ (001) superlattices. *Physical Chemistry Chemical Physics,* **2020**, *22* (10): 5826–5831.

[36] Gu T, Scarbrough T, Yang Y, et al. Cooperative couplings between octahedral rotations and ferroelectricity in perovskites and related materials. *Physical Review Letters,* **2018**, *120* (19): 197602.

[37] Rondinelli J M, Spaldin N A. Structure and properties of functional oxide thin films: Insights from electronic–structure calculations. *Advanced Materials,* **2011**, *23* (30): 3363–3381.

[38] Koohfar S, Disa A S, Marshall M S J, et al. Structural distortions at polar manganite interfaces. *Physical Review B,* **2017**, *96* (2): 024108.

[39] Zhang S, Guo X, Tang Y, et al. Polarization rotation in ultrathin ferroelectrics tailored by interfacial oxygen octahedral coupling. *ACS Nano,* **2018**, *12* (4): 3681–3688.

[40] Chen B, Gauquelin N, Green R J, et al. Spatially controlled octahedral rotations and metal-insulator transitions in nickelate superlattices. *Nano Letters,* **2021**, *21* (3): 1295–1302.

[41] Kan D, Anada M, Wakabayashi Y, et al. Oxygen octahedral distortions in compressively strained $SrRuO_3$ epitaxial thin films. *Journal of Applied Physics,* **2018**, *123* (23): 235303.

[42] Chen P F, Lan D, Liu C, et al. Correlated cation lattice symmetry and oxygen octahedral rotation in perovskite oxide heterostructures. *Journal of Applied Physics,* **2021**, *129* (2): 025303.

[43] Muller D A. Structure and bonding at the atomic scale by scanning transmission electron microscopy. *Nature Materials,* **2009**, *8* (4): 263–270.

[44] Ovsyannikov S V, Abakumov A M, Tsirlin A A, et al. Perovskite-like Mn_2O_3: A path to new manganites. *Angewandte Chemie International Edition,* **2013**, *52* (5): 1494–1498.

[45] Bindu R, Pandey S K, Kumar A, et al. Local distortion of MnO_6 octahedron in $La_{1-x}Sr_xMnO_{3+\delta}$ (x = 0.1–0.9): An EXAFS study. *Journal of Physics: Condensed Matter,* **2005**, *17* (41): 6393–6404.

[46] Bashir J, Shaheen R, Khan M N. Structural characterization of $SrLaMnRuO_6$ by synchrotron X-ray powder diffraction and X-ray absorption spectroscopy. *Solid State Sciences,* **2008**, *10* (5): 638–644.

[47] Shaheen R, Bashir J, Khan M N. EXAFS studies of ruthenium based double perovskite $ALaMnRuO_6$ (A = Ca, Sr, Ba). *Materials Sciences and Applications,* **2012**, *03* (01): 24–29.

[48] Mahana S, Manju U, Nandi P, et al. Role of local structural distortion in driving ferroelectricity in $GdCrO_3$. *Physical Review B,* **2018**, *97* (22): 224107.

[49] Jiang Y, Yuan L, Wang X, et al. Jahn-Teller disproportionation induced exfoliation of unit-cell scale ε-MnO_2. *Angewandte Chemie International Edition,* **2020**, *59* (50): 22659–22666.

[50] Yuan Y K, Lu Y F, Stone G, et al. Three-dimensional atomic scale electron density reconstruction of octahedral tilt epitaxy in functional perovskites. *Nature Communications,* **2018**, *9*: 5220.

[51] Herger R, Willmott P R, Schleputz C M, et al. Structure determination of monolayer-by-monolayer grown $La_{1-x}Sr_xMnO_3$ thin films and the onset of magnetoresistance. *Physical Review B,* **2008**, *77* (8): 085401.

[52] Bielecki J, Svedlindh P, Tibebu D T, et al. Structural and magnetic properties of isovalently substituted multiferroic $BiFeO_3$: Insights from Raman spectroscopy. *Physical Review B,* **2012**, *86* (18): 184422.

[53] Xu Q, Zheng X, Wen Z, et al. Enhanced room temperature ferromagnetism in porous $BiFeO_3$ prepared using cotton templates. *Solid State Communications,* **2011**, *151* (8): 624–627.

[54] Iliev M, Abrashev M, Lee H-G, et al. Raman spectroscopy of orthorhombic perovskitelike YMnO₃ and LaMnO₃. *Physical Review B*, **1998**, *57* (5): 2872.

[55] Woodward P M, Cox D E, Moshopoulou E, et al. Structural studies of charge disproportionation and magnetic order in CaFeO₃. *Physical Review B*, **2000**, *62* (2): 844–855.

[56] Medarde M, Fernandez-Diaz M T, Lacorre P. Long-range charge order in the low-temperature insulating phase of PrNiO₃. *Physical Review B*, **2008**, *78* (21): 212101.

[57] Blasco J, Rodriguez-Velamazan J A, Garcia J, et al. Structural properties of charge disproportionation and magnetic order in Sr₂/₃Ln₁/₃FeO₃ (Ln=La, Pr, and Nd). *Physical Review B*, **2018**, *98* (10): 104422.

[58] Cheng J, Kweon K E, Larregola S A, et al. Charge disproportionation and the pressure-induced insulator-metal transition in cubic perovskite PbCrO₃. *Proceedings of the National Academy of Sciences of the United States of America*, **2015**, *112* (6): 1670–1674.

[59] Azuma M, Carlsson S, Rodgers J, et al. Pressure-induced intermetallic valence transition in BiNiO₃. *Journal of the American Chemical Society*, **2007**, *129* (46): 14433–14436.

[60] Leonov I, Belozerov A S, Skornyakov S L. Unusual Mott transition associated with charge-order melting in BiNiO₃ under pressure. *Physical Review B*, **2019**, *100* (16): 161112(R).

[61] Alonso J A, Garcia-Munoz J L, Fernandez-Diaz M T, et al. Charge disproportionation in RNiO₃ perovskites: Simultaneous metal-insulator and structural transition in YNiO₃. *Physical Review Letters*, **1999**, *82* (19): 3871–3874.

[62] Hong S S, Gu M, Verma M, et al. Extreme tensile strain states in La₀.₇Ca₀.₃MnO₃ membranes. *Science*, **2020**, *368* (6486): 71–76.

[63] Alexe M, Ziese M, Hesse D, et al. Ferroelectric switching in multiferroic magnetite Fe₃O₄ thin films. *Advanced Materials*, **2009**, *21* (44): 4452–4455.

[64] Ikeda N, Ohsumi H, Ohwada K, et al. Ferroelectricity from iron valence ordering in the charge-frustrated system LuFe₂O₄. *Nature*, **2005**, *436* (7054): 1136–1138.

[65] Elfimov I S, Anisimov V I, Sawatzky G A. Orbital ordering, Jahn-Teller distortion, and anomalous X-ray scattering in manganates. *Physical Review Letters*, **1999**, *82* (21): 4264–4267.

[66] Halcrow M A. Jahn-Teller distortions in transition metal compounds, and their importance in functional molecular and inorganic materials. *Chemical Society Reviews*, **2013**, *42* (4): 1784–1795.

[67] Murakami Y, Hill J, Gibbs D, et al. Resonant x-ray scattering from orbital ordering in LaMnO₃. *Physical Review Letters*, **1998**, *81* (3): 582.

[68] Cohen R E. Origin of ferroelectricity in perovskite oxides. *Nature*, **1992**, *358* (6382): 136–138.

[69] Hill N A. Why are there so few magnetic ferroelectrics? *Journal of Physical Chemistry B*, **2000**, *104* (29): 6694–6709.

[70] Huijben M, Koster G, Liao Z, et al. Interface-engineered oxygen octahedral coupling in manganite heterostructures. *Applied Physics Reviews*, **2017**, *4* (4): 041103.

[71] Kim T H, Puggioni D, Yuan Y, et al. Polar metals by geometric design. *Nature*, **2016**, *533* (7601): 68–72.

[72] Liao Z, Gauquelin N, Green R J, et al. Metal-insulator-transition engineering by modulation tilt-control in perovskite nickelates for room temperature optical switching. *Proceedings of the National Academy of Sciences of the United States of America*, **2018**, *115* (38): 9515–9520.

[73] Dong Y, Ma Z, Luo Z, et al. Interfacial octahedral manipulation imparts hysteresis-free metal to insulator transition in ultrathin nickelate heterostructure. *Advanced Materials Interfaces*, **2019**, *6* (17): 1900644.

[74] Zhai X, Cheng L, Liu Y, et al. Correlating interfacial octahedral rotations with magnetism in (LaMnO₃₊δ)ₙ/(SrTiO₃)ₙ superlattices. *Nature Communications*, **2014**, *5*: 4283.

[75] Guan X, Shen X, Zhang J, et al. Tuning magnetism and crystal orientations by octahedral coupling in LaCoO₃/LaMnO₃ thin films.

[76] Ziese M, Jin L, Lindfors-Vrejoiu I. Unconventional anomalous Hall effect driven by oxygen-octahedra-tailoring of the SrRuO₃ structure. *Journal of Physics:Materials*, **2019**, *2* (3): 034008.

[77] Qin Q, Liu L, Lin W, et al. Emergence of topological Hall effect in a SrRuO₃ single layer. *Advanced Materials*, **2019**, *31* (8): e1807008.

[78] Gu Y, Wei Y-W, Xu K, et al. Interfacial oxygen-octahedral-tilting-driven electrically tunable topological Hall effect in ultrathin SrRuO₃ films. *Journal of Physics D:Applied Physics*, **2019**, *52* (40): 404001.

[79] Kim J R, Jang J, Go K J, et al. Stabilizing hidden room-temperature ferroelectricity via a metastable atomic distortion pattern. *Nature Communications*, **2020**, *11* (1): 4944.

[80] Wang H, Tang F, Stengel M, et al. Convert widespread paraelectric perovskite to ferroelectrics. *Physical Review Letters*, **2022**, *128* (19): 197601.

[81] Burdett J K. Similarities in the structural chemistry of d⁸ and d⁹ transition metal complexes. Explanation in terms of the angular overlap model. *Inorganic Chemistry*, **1975**, *14* (4): 931–934.

[82] Liu H, Dong Y, Xu D, et al. Dynamic field modulation of the octahedral framework in metal oxide heterostructures. *Advanced Materials*, **2018**, *30* (52): e1804775.

[83] Cammarata A, Rondinelli J M. Octahedral engineering of orbital polarizations in charge transfer oxides. *Physical Review B*, **2013**, *87* (15): 155135.

[84] Tannous C, Gieraltowski J. The Stoner-Wohlfarth model of ferromagnetism. *European Journal of Physics*, **2008**, *29* (3): 475–487.

[85] Zener C. Interaction between the d-shells in the transition metals. II. Ferromagnetic compounds of manganese with perovskite structure. *Physical Review*, **1951**, *82* (3): 403.

[86] Zhang B, Wu L, Feng X, et al. Tuning irreversible magnetoresistance in Pr₀.₆₇Sr₀.₃₃MnO₃ film via octahedral rotation. *ACS Applied Materials & Interfaces*, **2020**, *12* (38): 43222–43230.

[87] Nagaosa N, Tokura Y. Topological properties and dynamics of magnetic skyrmions. *Nature Nanotechnology*, **2013**, *8* (12): 899–911.

[88] Neubauer A, Pfleiderer C, Binz B, et al. Topological Hall effect in the a phase of MnSi. *Physical Review Letters*, **2009**, *102* (18): 186602.

[89] Ohnishi T, Takada K. Epitaxial thin-film growth of SrRuO₃, Sr₃Ru₂O₇, and Sr₂RuO₄ from a SrRuO₃ target by pulsed laser deposition. *Applied Physics Express*, **2011**, *4* (2): 025501.

[90] Lin S, Zhang Q, Sang X, et al. Dimensional control of octahedral tilt in SrRuO₃ via infinite-layered oxides. *Nano Letters*, **2021**, *21* (7): 3146–3154.

[91] Pramanick A, Paterson A, Denis L, et al. Oxygen octahedral tilt ordering in (Na₁/₂Bi₁/₂)TiO₃ ferroelectric thin films. *Applied Physics Letters*, **2020**, *116* (2): 022902.

[92] Benedek N A, Fennie C J. Why are there so few perovskite ferroelectrics? *Journal of Physical Chemistry C*, **2013**, *117* (26): 13339–13349.

[93] Geng W R, Guo X W, Zhu Y L, et al. Oxygen octahedral coupling mediated ferroelectric-antiferroelectric phase transition based on domain wall engineering. *Acta Materialia*, **2020**, *198*: 145–152.

[94] Liao Z, Gauquelin N, Green R J, et al. Thickness dependent properties in oxide heterostructures driven by structurally induced metal-oxygen hybridization variations. *Advanced Functional Materials*, **2017**, *27* (17): 1606717.

[95] Yi D, Flint C L, Balakrishnan P P, et al. Tuning perpendicular magnetic anisotropy by oxygen octahedral rotations in (La₁₋ₓSrₓMnO₃)/(SrIrO₃) superlattices. *Physical Review Letters*, **2017**, *119* (7): 077201.

[96] Zhang J, Zhong Z, Guan X, et al. Symmetry mismatch-driven perpendicular magnetic anisotropy for perovskite/brownmillerite heterostructures. *Nature Communications*, **2018**, *9*: 1923.

[97] Meng M, Wang Z, Fathima A, et al. Interface-induced magnetic polar metal phase in complex oxides. *Nature Communications*, **2019**, *10*: 5248.